

# Biplane Correlation Imaging: A Feasibility Study Based on Phantom and Human Data

Ehsan Samei · Nariman Majdi-Nasab ·  
James T. Dobbins III · H. Page McAdams

Published online: 27 May 2011  
© Society for Imaging Informatics in Medicine 2011

**Abstract** The objective of this study was to implement and evaluate the performance of a biplane correlation imaging (BCI) technique aimed to reduce the effect of anatomic noise and improve the detection of lung nodules in chest radiographs. Seventy-one low-dose posterior–anterior images were acquired from an anthropomorphic chest phantom with  $0.28^\circ$  angular separations over a range of  $\pm 10^\circ$  along the vertical axis within an 11 s interval. Similar data were acquired from 19 human subjects with institutional review board approval and informed consent. The data were incorporated into a computer-aided detection (CAD) algorithm in which suspect lesions were identified by examining the geometrical correlation of the detected signals that remained relatively constant against variable anatomic backgrounds. The data were analyzed to determine the effect of angular separation, and the overall sensitivity and false-positives for lung nodule

detection. The best performance was achieved for angular separations of the projection pairs greater than  $5^\circ$ . Within that range, the technique provided an order of magnitude decrease in the number of false-positive reports when compared with CAD analysis of single-view images. Overall, the technique yielded  $\sim 1.1$  false-positive per patient with an average sensitivity of 75%. The results indicated that the incorporation of angular information can offer a reduction in the number of false-positives without a notable reduction in sensitivity. The findings suggest that the BCI technique has the potential for clinical implementation as a cost-effective technique to improve the detection of subtle lung nodules with lowered rate of false-positives.

**Keywords** Computer-aided detection · Biplane correlation imaging · Lung nodules · Chest radiography

E. Samei · N. Majdi-Nasab · J. T. Dobbins III · H. P. McAdams  
Carl E. Ravin Advanced Imaging Laboratories,  
Department of Radiology, Duke University,  
Durham, NC 27710, USA

E. Samei · J. T. Dobbins III  
Department of Biomedical Engineering, Duke University,  
Durham, NC 27710, USA

E. Samei · J. T. Dobbins III  
Medical Physics Graduate Program, Duke University,  
Durham, NC 27710, USA

E. Samei  
Department of Physics, Duke University,  
Durham, NC 27710, USA

E. Samei (✉)  
Duke University Medical Center,  
2424 Erwin Road, Suite 302 (DUMC Box 2731),  
Durham, NC 27705, USA  
e-mail: samei@duke.edu

## Introduction

Lung cancer is a leading cause of death in the United States, surpassing the mortality rate of colon, breast, and prostate cancers combined [1]. In its early stages, lung cancer may manifest itself as a solitary lung nodule. Unfortunately, many small lung nodules (and hence cancers) are not detected, even retrospectively, on chest radiographs [2, 3]. Even experienced radiologists have difficulty detecting subtle lung nodules [4]. Despite the many technological advances in chest radiography in the last five decades, there has been little improvement in the poor detection rate for small lung nodules [4–8].

There are three main factors limiting the detection of subtle lung nodules in chest radiographs: nodule signal-to-noise ratio (SNR), perceptual errors (both visual and cognitive), and anatomic noise. The accurate identification

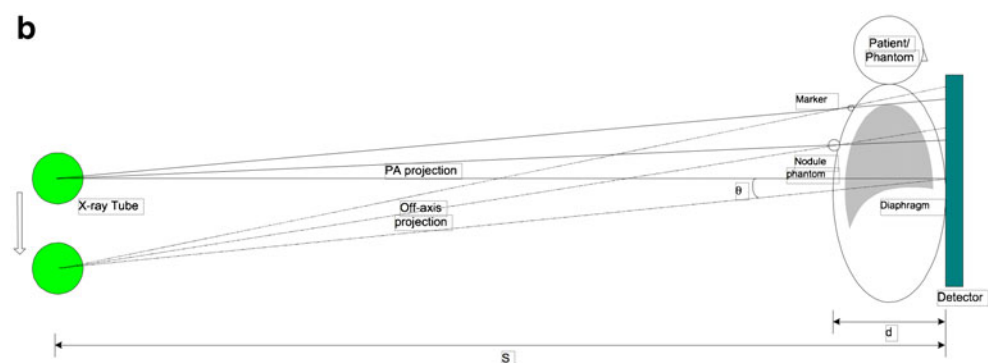
of lung nodules can be hindered by their low SNR. Recent advancements in radiologic technology, including the development of high detective quantum efficiency digital radiographic systems, have enhanced the SNR for lung lesions. Perceptual errors also notably contribute to the poor detection rate of lung nodules [9–11]. Computer-assisted detection (CAD) algorithms can minimize the perceptual errors encountered in the detection of lung nodules by enabling a complete search of the image data [12–15]. The third and perhaps the most significant obstacle to the accurate detection of lung nodules remains the anatomic noise caused by the normal thoracic structures that surround and overlay a lesion, thus masking its appearance [16–19].

Multi-dimensional imaging techniques such as dual-energy subtraction radiography, tomosynthesis, or computed tomography (CT) can improve the detection of lung nodules by reducing the impact of anatomic noise on image interpretation [17]. As a new multi-dimensional imaging method, we recently introduced a new multi-projection imaging paradigm called correlation imaging (CI) that similarly attempts to reduce the impact of anatomic noise on the detection of subtle lung nodules [20, 21]. In CI, two or more digital images of the body part are acquired

within a short time interval from slightly different projections. The image data are then incorporated into an enhanced CAD algorithm that detects nodules by examining the geometrical correlation of the detected suspect regions in separate views. The technique helps to reduce the impact of anatomic noise and to minimize the number of CAD false-positives by eliminating non-correlated nodule candidates in the images. One particular implementation of CI, named biplane correlation imaging (BCI), only uses two views to achieve this objective [20, 22, 23]. CAD-BCI uses one projection image as a reference and another one to cancel out non-related suspicious regions. Both images are further used during the interpretation process by the radiologist.

In this paper, we report on one implementation of BCI. The study was primarily based on a set of off-angle projections acquired from an anthropomorphic chest phantom. The aim of the study was to assess the relative performance of BCI and CAD for lung nodule detection using three segmentation techniques, and to further ascertain an optimum angular projection for paired projection images such that the number of false-positives is minimized. The paper further reports the initial results of the technique on human subjects.

**Fig. 1** **a** The tomosynthesis machine (*left*) and anthropomorphic chest phantom (*right*) are shown during the imaging. For human data acquisition, the patient was positioned in the place of the chest phantom. **b** Schematic depiction of the BCI scheme



## Subjects and Methods

### Image Data

Multi-projection thoracic images were acquired on an imaging system designed for chest tomosynthesis [24] (Fig. 1). The system used was based on a custom-built prototype device containing a commercial-grade flat-panel detector (XQ/i; GE Medical Systems, Milwaukee, WI) capable of acquiring 14-bit chest images of  $2,048 \times 2,048$  matrix size and 0.2 mm pixel pitch. An anthropomorphic chest phantom (RSD, Inc., Long Beach, CA) was positioned in a standard chest posteroanterior (PA) position. Two Teflon nodule phantoms of 8 and 10 mm in diameter were placed on the phantom's posterior surface to simulate the appearance of subtle tissue-equivalent nodules [25]. The phantom was then imaged 71 times (120 kVp, 5 mAs), with the X-ray tube moving 64.2 cm along the vertical axis to acquire projection images with  $0.28^\circ$  angular separation over an angular range of  $\pm 10^\circ$ . The precise movement of the X-ray tube was achieved with a programmable tube mover.

The chest phantom was imaged multiple times with the positions of the added nodules randomly altered (the phantom remained fixed) to allow different superimposition of the nodule with the anatomy. Ten such image sets were acquired for testing, and one set was acquired to train the algorithm. However, the main purpose of the project was to develop the methodology as opposed to conducting an independent testing of the BCI algorithm. Positions of added nodules were different among image sets but fixed within each image set. An additional set of images without nodule phantoms was also acquired, which was then subtracted from the main dataset to determine exact nodule locations in the dataset.

BCI was also evaluated on a set of human subject data, collected from outpatients at Duke University Medical Center using an institutional review board-approved protocol. All human subjects were previously diagnosed with lung nodules, and patients recruited for this study were limited to those who were coming for a CT follow-up and had nodules 3–21 mm in diameter. Nineteen consented subjects (ten males, nine females, 33–73 years; mean, 59 years) participated in the study. Each subject underwent a standard posterior–anterior radiographic image acquisition, as well as a multi-projection image acquisition. The protocol for the first five human subjects involved 61 angular projections within the  $\pm 10^\circ$  angular range. The remaining subjects were imaged using the same protocol as that of the phantom. Each projection image used an X-ray exposure equivalent to 1/11 of a conventional PA. Thus, the total X-ray dose for BCI imaging (using two of the collected projections in the implementation of this study) was about 1/7th of a conventional PA. During X-ray exposure, subjects were required to remain still and hold their breath for the 10–12 s duration of the acquisition. An experienced chest

radiologist marked all nodules on conventional PA images based on the associated CT dataset establishing ground truth. Seventy-two nodules (3–21 mm in diameter; mean, 7.8 mm) were identified in the 19 human subjects.

### Computer Analysis

All images were processed through our biplane image analysis method, summarized in Fig. 2. The sections below provide a step-by-step summary of the processes. All image analyses were performed on a Pentium-class workstation using MATLAB<sup>®</sup> (The Mathworks, Inc., Natick, MA) software package.

#### Image Filtration

Each projection image was first pre-processed and its intensities scaled to 16 bits pixel intensity. That included a baseline subtraction of the minimum pixel value within a  $140 \times 40$  mm<sup>2</sup> region of interest in the right lung from each of the projection images. The projection image data were then down-sampled to  $1,024 \times 1,024$  matrix size. This was found to reduce computational time without negatively impacting the detection of nodules. The noise within the images was also reduced using a Wiener filter [26] with a mask size of  $1.2 \times 1.2$  mm<sup>2</sup>.

Since lung nodules generally follow a Gaussian-type profile [17], a Gaussian-based normalized cross-

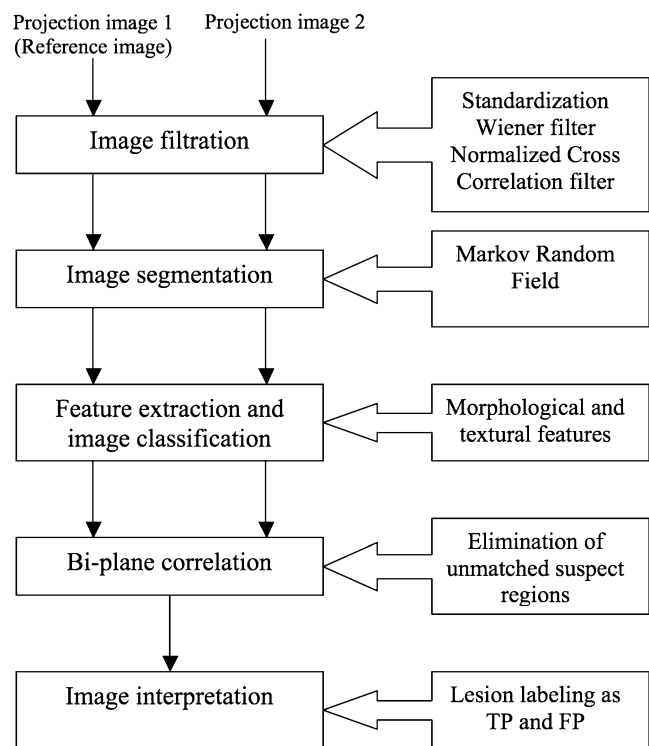


**Fig. 2** Schematic of the computerized detection of the nodules

correlation filter was applied [20, 27] to enhance the nodule-like features of the images. The filter required three parameters to be specified: template filter size and the two standard deviations of the constituent Gaussians. Empirical examinations for sets of kernel sizes and standard deviations indicated that a template filter size of  $409.6 \times 409.6 \text{ mm}^2$  and standard deviations of 1.6 and 4.8 mm would optimally enhance the desired features of the nodules. The output of the filtration was an image with values ranging between  $-1$  and  $1$ , with the extremes corresponding to a perfect match or mismatch of the original image to the likely nodules.

### Image Segmentation

Segmentations of the suspect regions followed the filtration process. Initially, the lung region of each original projection image was classified based on a histogram distribution of pixel values in the filtered image. The number of classes in the segmentation images varied among projection images as a result of differences in the gray-level distribution of the filtered image. Label pixels of each class were set so that each class would differ from its two adjacent classes by seven pixels. The classification results were used in a segmentation scheme based on a stochastic model inspired by Markov random field (MRF). The MRF process adaptively segmented the images based the number of the regions. MRF provides a convenient and consistent way for modeling context-dependent entities such as image pixels and correlated features by characterizing the mutual influence among such entities [28, 29] (Hammersley and Clifford, unpublished). In our approach, an approximate maximum a posteriori estimate of the field was used to segment the image [30].

To increase image segmentation's contribution to accurate nodule detection, we evaluated three segmentation methods based on MRF: minimum gray-level distance (MGLD), simulated annealing (SA), and thresholding (THRE), in which a histogram of the filtered image was equally separated into different sections and each section assigned to only one gray-level (class) [31, 32]. All three methods used the second-order clique potential and the same a priori information. The MRF model's  $\beta$  value, a parameter enabling adjustments of the relative importance of smoothness of the regions in the segmentation process, was set to an optimum value of 0.2 based on prior works [31, 32].

### Feature Extraction

Once suspect regions were identified through the previous stage, their features were examined. At the outset, regions were passed through an unsharp masking filter [33] to enhance their high-frequency components around

edges. Furthermore, radius of nodule candidates that fell outside of the target range of 3 to 21 mm in diameter was discarded. Radius was measured as root of total area of nodule candidate divided by constant number  $\pi$ . From each of the remaining suspicious candidates, 34 features were measured. The interdependencies of the features were then examined and the features found correlated or unstable removed from further consideration for final classifier using free-response operating characteristic (FROC) methodology. From the initial set of 34 features, 12 survived this selection process. Those included six morphological features and six textural features, as listed in Table 1.

Those features were used to eliminate false-positives by evaluating the growth of suspect regions using a method similar to Giger et al. [12]. Eventually, a 12-dimensional threshold on the feature classifier outputted a binary decision on each suspect candidate. The final outcome of the feature extraction stage was an image

**Table 1** The features used to characterize the suspicious regions in the filtered images

Morphological features
Ratio of the region area to the smallest convex polygon that encloses the entire region
Ratio of the biggest and smallest eigenvalues of the region
Ratio of the region area to the area of the enclosing bounding box
Fraction of the region coincident with a circle of equivalent area centered at the region's centroid
Average of radial length, defined as a normalized distance from the region's centroid to each of its boundary points, as $\mu_{r_l} = \frac{1}{N} \sum_{i=1}^N r_i$ , where $r_i$ is the radial length to the $i$ th boundary point and $N$ is the number of boundary points.
Entropy of radial distance length as the degree of randomness of radial length [51]
Textual features
Dissimilarity as the difference between average gray levels of the exterior and interior regions to their sum, as $\text{Dissimilarity} = \frac{\mu_{\text{Int}} - \mu_{\text{Ext}}}{\mu_{\text{Int}} + \mu_{\text{Ext}}}$ , where $\mu_{\text{Int}}$ and $\mu_{\text{Ext}}$ are the region's average interior and exterior gray levels, respectively. The exterior region was considered to be the portion of the image not contained within the region but two times bigger than the radial lengths of the region with the same centroid.
Average of gray-level difference between the center pixel of a region and its boundary pixels, defined as $AG = \frac{1}{N} \sum_{i=1}^N (P_{\text{Center}} - P_r)$ , where $N$ is the number of boundary points and $P_{\text{Center}}$ and $P_r$ are the gray levels at a region's center and the $i$ th boundary point, respectively.
Co-occurrence matrix parameters of the region in terms of contrast, correlation, energy, and homogeneity [52]. The co-occurrence matrix was calculated as the interaction between gray values of pixels separated by the distance of the biggest eigenvalue of the region at angles of $0^\circ$ , $45^\circ$ , $90^\circ$ , and $135^\circ$ .

which mapped the location and extent of suspect regions (i.e., potential lung nodules) in each of the projection images.

#### *Biplane Correlation Method*

BCI reduced the number of false-positive nodules by correlating the presence of suspect nodules found in projection image pairs. A suspect candidate in a projection image was first mapped to its potential location in the reference projection; in this study, given the angular separation between the two views,  $\theta$ , and maximum measured thickness of the thorax,  $d$ , a correlation rectangle was defined in the reference image within which the nodule could be maximally projected [20]. The height of the rectangle was calculated as  $d \tan(\theta)$ . The width of the rectangle was assumed to be variable and equal to the effective diameter of the suspect nodule under examination. If a corresponding suspect lesion was found in the correlation rectangle in the reference image, the match was marked as a positive outcome; otherwise, it was discarded from further consideration.

#### *Image Interpretation*

Alternatively, to evaluate the performance of the BCI technique, all suspect regions in each of the projection images were compared against their truth files, indicating the location of actual lesions in the images. The truth files for the phantom images were generated by subtracting each image from a corresponding image at the same projection angle but without nodules. The truth files for the human images were generated based on the associated CT dataset. A true-positive (TP) was recorded if there was any overlap between a detected nodule and a true nodule; otherwise the nodule found was recognized as a false-positive (FP).

#### *Angular Separation Effect*

As an important acquisition parameter, we examined the effect of angular separation on the BCI performance. To do so, PA projections were paired with individual oblique projection images across  $6 \pm 1^\circ$ ,  $5 \pm 1^\circ$ ,  $4 \pm 1^\circ$ ,  $3 \pm 1^\circ$ ,  $2 \pm 1^\circ$ ,  $1 \pm 1^\circ$ , and  $0 \pm 1^\circ$  degree off-axis angular ranges, and

**Fig. 3** Sample phantom and human images acquired at  $-10^\circ$  (a, c) and  $+10^\circ$  (b, d) projections. The phantom images (a, b) include two added nodules, 8 and 10 mm in diameter. The human images (c, d) are from a middle-aged woman with a history of breast cancer and a right partial mastectomy. An 8-mm nodule can be seen in the left lung of the subject

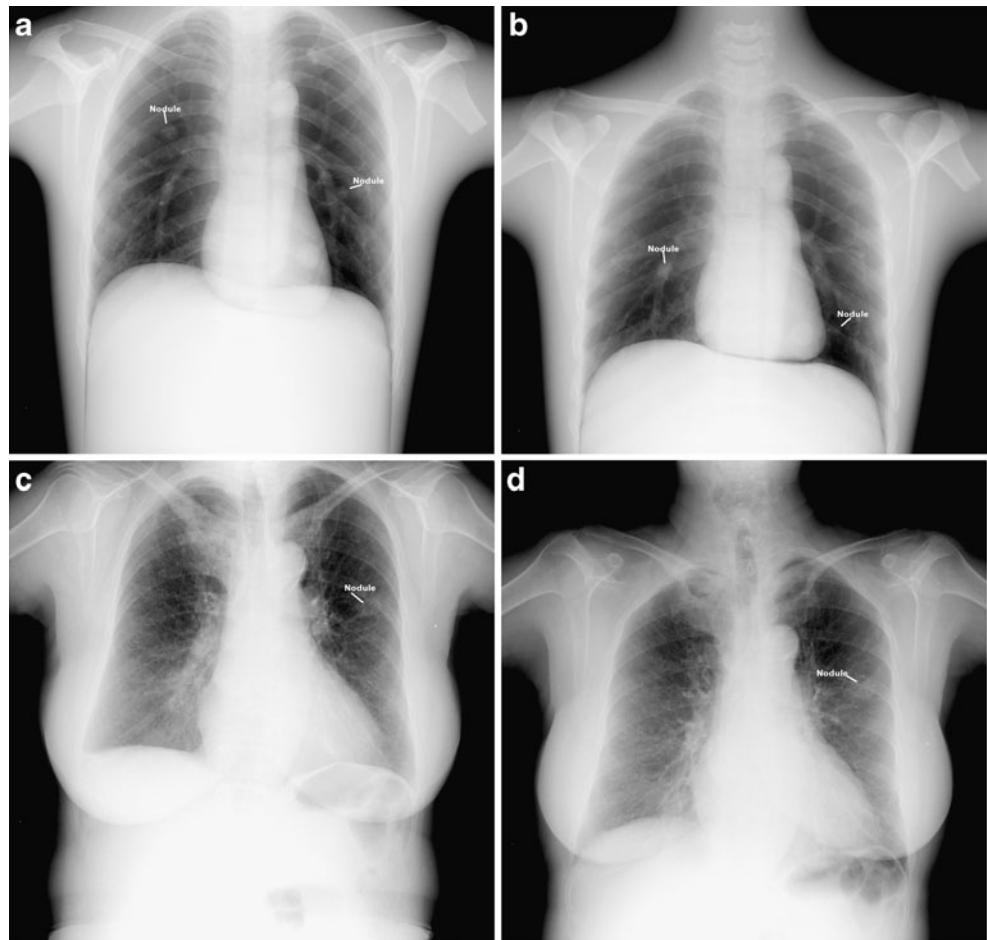
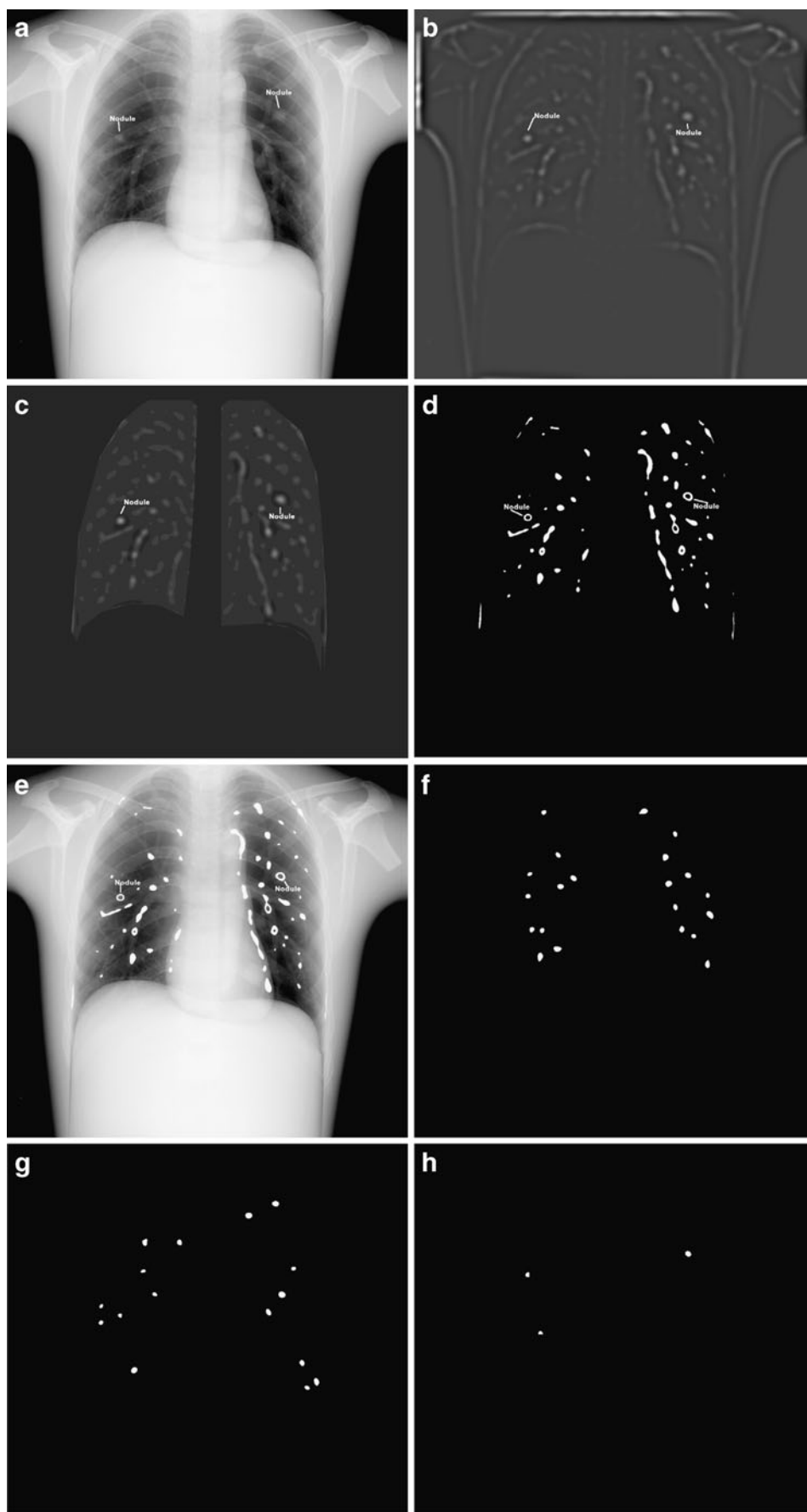


**Fig. 4** A sample projection image (a) and its resultant image filtration output (b). Nodules are marked on both images. The following images show the output of the image segmentation of the filtered image (c), and the fifth class of the segmented image (d), with region locations identified on the original projection image (e). Feature extraction outcome of the image (f) is matched against that from the PA image (g) to render the final BCI outcome (h) indicating two true-positives (*upper marks*) and one false-positive (*the lower mark*)



results for the images across those ranges averaged. The performance was then characterized by FROC analysis [34] in terms of the number of TPs and FPs for each of the projection pairs within those ranges.

## Results

Figure 3 illustrates representative phantom and patient images obtained in our study. The examples are at the extremes of the angular range, exhibiting the maximum vertical displacement of the projected nodules. Figure 4 shows workflow results of CAD–BCI on phantom images. CAD is applied to all projection images while BCI finalizes the results by paring the projection images with PA projection image.

Figure 5 illustrates the outcome of the computer analyses of the images, when applied (a) to single images and (b) to image pairs according to the BCI scheme, where each angular projection is paired with that of the PA view. In either case, the number of true-positives remains relatively stable regardless of the angular projection, indicating almost perfect sensitivity (i.e., both of the two nodules in this case are detected in almost each single projection images regardless of the angle). However, the number of false-positives varies significantly. For the case of single-view analysis, it averages to about 18 per image and is higher for positive projection angles. For BCI analysis (Fig. 5b), the number of false-positive is highly dependent on the projection angle of the image being paired with the PA view. For the smallest angle (i.e.,  $0.28^\circ$ ), that amounts to 14 (i.e., the false-positive peak in Fig. 5b). However, larger angles cause a notable reduction in that number, enabling almost perfect specificity at the largest angles (i.e., zero or one false-positive at the left and right extremes of Fig. 5b).

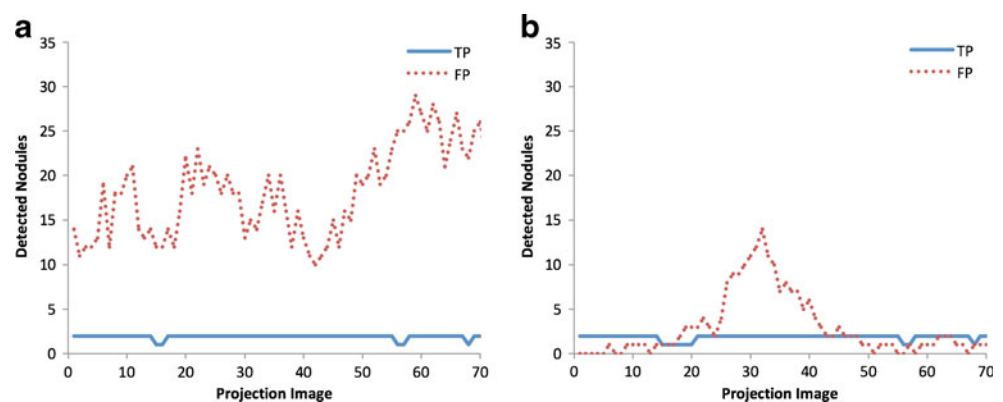
Trends similar to that of the phantom data can be appreciated for human subjects as well, as illustrated in Fig. 6. The only differences are in the false-positive trend for single-view analysis as a function of projection angle, and the number of false-positives being generally higher for the BCI technique, primarily due the presence of more anatomic

noise in the human subject data. Nonetheless, a notable reduction of false-positives is observed at larger angular projections. As a typical example, in Fig. 6a, the single-view analysis of image 49 ( $+6^\circ$  projection angle) yielded one true-positive and 18 false-positives. The BCI analysis of that image paired with the PA view reduced the number of false-positives to two, with no impact on true-positives (i.e., unchanged true-positive line across angles in Fig. 6b). The phantom and human dataset results demonstrate very effective removal of false-positives by the BCI scheme, with no or little impact on the number of true-positives and on sensitivity. Similar results were obtained when reference image was one of the oblique projections as opposed to PA.

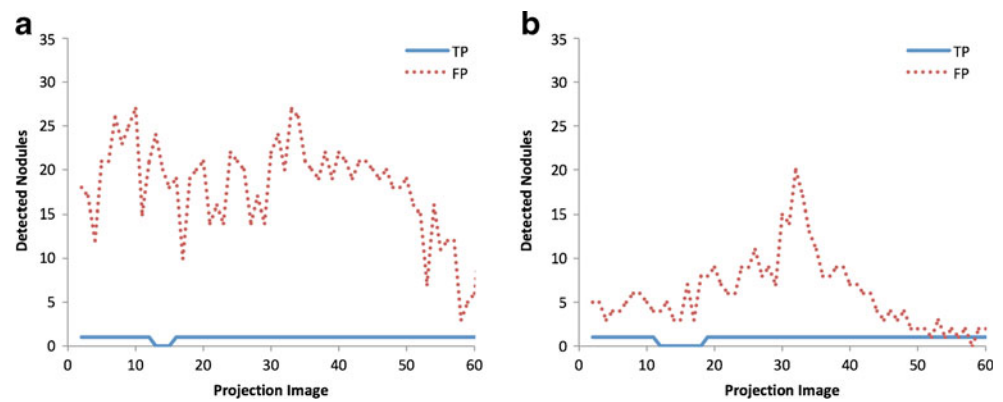
The choice of segmentation technique showed a small effect on the results proving robustness of BCI in removing false candidates. Figure 7 illustrates representative results. Overall, the MGLD technique yielded a slightly more favorable number of false-positives without affecting sensitivity. Computational times for the three techniques examined, THRE, SA, and MGLD, were approximately 0.4, 5, and 1 min, respectively. In spite of a less favorable computational time, MGLD was selected for image segmentation due to its slightly superior performance compared with the other methods.

Figure 8 shows the impact of angular separation on the BCI performance for phantom images, expressed in terms of FROC curves. The performance was plotted for both (a) negative angular projections from  $-10^\circ$  to  $-1^\circ$  and (b) positive angular projections from  $+1^\circ$  to  $+10^\circ$ . The results indicate that, for any angular separation, more sensitivity will “cost” more in terms of the number of false-positives. However, that trade-off is more favorable at larger angular separations. At an operational zone of the FROC, Fig. 9 illustrates the number true-positives and false-positives as a function of angular separation. The results indicate optimum performance in terms of false-positive reduction when the angular separation of the projection pair is greater than  $5^\circ$ . Operating in this range, one may achieve an average of about 1.1 FPs per image pair at a sensitivity level of 75%.

**Fig. 5** **a** Shows our single-view CAD results in terms of the number of false-positives and true-positives obtained from 71 projection images of the chest phantom containing two lung nodules. Projections 1 to 71 correspond to the angular range of  $-10^\circ$  and  $+10^\circ$ . **b** Illustrates the BCI results when each image was correlated with the PA projection. The algorithms used MGLD segmentation



**Fig. 6** **a** Shows our single-view CAD results in terms of the number of false-positives and true-positives obtained from 61 projection images of a human subject containing one lung nodule. Projections 1 to 61 correspond to the angular range of  $-10^\circ$  and  $+10^\circ$ . **b** Illustrates the BCI results when each image was correlated with the PA projection. The algorithms used MGLD segmentation



## Discussion

Several promising methods have been developed to reduce the influence of anatomic noise in thoracic radiography. Two such techniques that aim to improve lung nodule detection by minimizing the appearance of ribs and other overlaying thoracic structures are dual-energy subtraction imaging [35, 36] and digital tomosynthesis [37, 38]. Both techniques have systems commercially available, and their clinical utilization is evolving. CT is probably the optimal modality for minimizing anatomic noise in chest imaging as it eliminates the overlays of most anatomic structures associated with projection imaging. While the use of low-dose CT for lung cancer screening is under investigation [39–43] at present, utilization of CT as a widespread screening method for the detection of subtle lung nodules is controversial because of associated economic (cost and technology availability), patient care (e.g., over-diagnosis), and patient dose concerns.

The underlying hypothesis of correlation imaging is that the anatomic noise associated with normal anatomic features in the thorax is the main factor limiting the detection of subtle lung nodules. With CI, angular information is used to minimize this limiting influence by identifying and positively

reinforcing the nodule signals, which remain relatively constant against a variation in the background structure.

Incorporating a robust CAD with BCI technique can notably lower the number of false nodule candidates. This approach does not promise to eliminate anatomic noise (as CT does), but it does aim to cost-effectively reduce its influence without an increase in patient dose. This paper reports on a particular implementation of the technique with the use of only two images, i.e., BCI. The implementation of BCI technique is feasible and inexpensive. The device that has been used in this study at Duke University Medical Center is a home-build modification of standard conventional PA X-ray machine. A precise step motor was added to X-ray tube to control projection beams. The study yielded highly encouraging results, demonstrating that it is possible to substantially reduce the number of false-positives in the projection data due to anatomic noise without a notable reduction in the number of true-positive marks. The findings suggest that the BCI technique has the potential for a CAD clinical implementation as a cost-effective technique for improving the detection of lung cancer.

This work parallels two prior works in the literature. Samei et al. reported on a multi-projection implementation of CI for

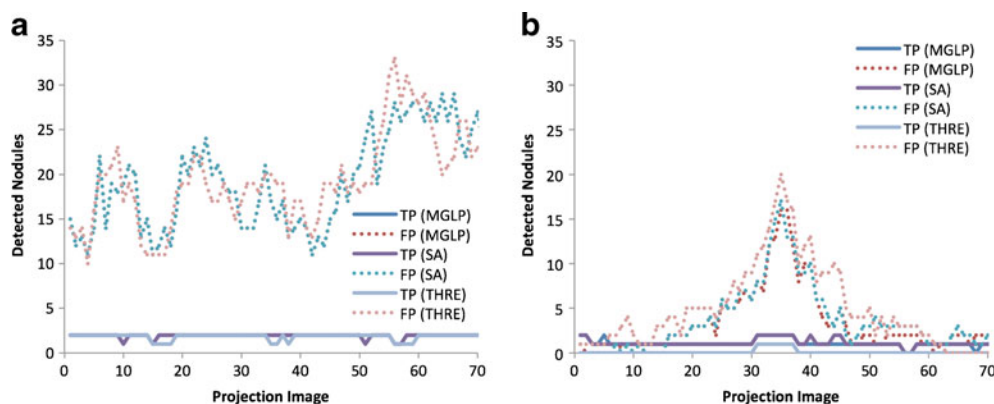
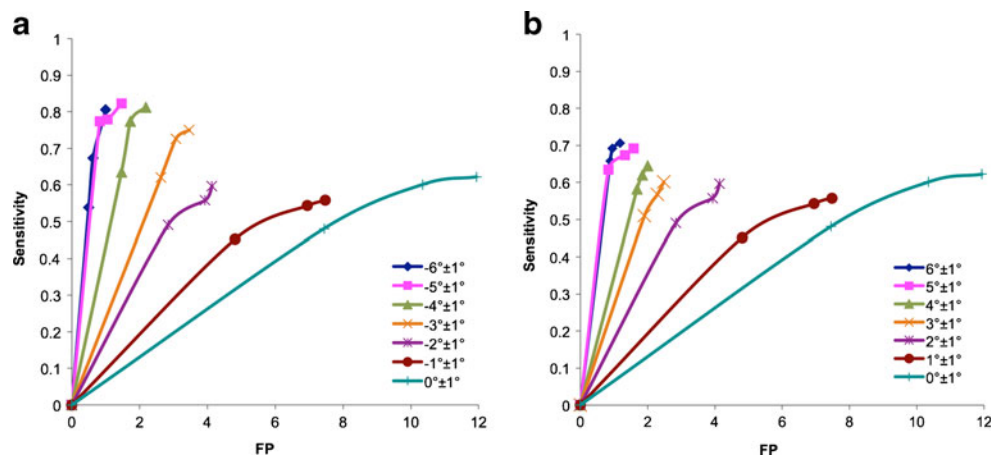


**Fig. 7** **a** Shows our single-view CAD results in terms of the number of false-positives and true-positives obtained from 71 projection images of the chest phantom containing two lung nodules. Projections 1 to 71 correspond to the angular range of  $-10^\circ$  and  $+10^\circ$ . **b** Illustrates

the BCI results when each image was correlated with the PA projection. The curves reflect the performance obtained with our three segmentation techniques: thresholding (*THRE*), minimum gray-level distance (*MGLD*), and simulated annealing (*SA*)

**Fig. 8** FROC analysis results of the average BCI performance, for negative angular projections (a) and positive angular projections (b), when each image was correlated with the PA image. The X-axis provides the number of false-positives per pair of images used for BCI processing



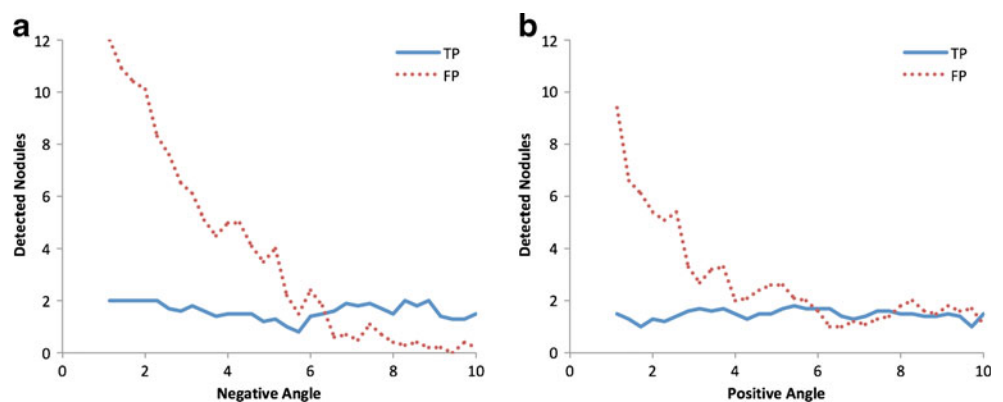
lung nodule detection [21]. Both studies indicate that the use of more than two projections enables an effective reduction of the influence of anatomic noise on CAD system performance. Reiser et al. used a somewhat different multi-projection approach, oriented particularly to breast projection images [44]. They aimed to explicitly develop a three-dimensional CAD approach using more than two projection images with dose levels associated with each projection lower than what might be used in BCI. For either study, the enhanced reduction of anatomic noise enabled with the use of additional projections needs to be placed in perspective with the additional dose that the approach might entail.

An essential element of BCI is the CAD algorithm used to process the projection images. We developed a CAD algorithm taking advantage of both the morphological and textual features of chest images to identify lung nodules. Our technique is similar to some prior implementations of CAD for chest radiography [45–50]. However, our approach differs from prior implementations in two significant ways. First, image segmentation was achieved through characterizing the mutual influence among MRF probabilities. This segmentation technique is less sensitive to the noise as it relies on neighborhood pixels. Segmentations were further done individually for each projected image. Secondly, the feature

selections went through a comprehensive search analysis to ensure their optimum utilization for CAD.

In spite of positive findings, our study had four limitations. One had primarily to do with the BCI technique itself for nodules located near periphery of the lungs. In angulated projections, these lesions can be shifted to areas outside of “foot-print” of the lungs, thus decreasing the detection accuracy of the technique. Extending CAD processing to areas outside of the lung regions of the projection images may solve this problem. Secondly, the BCI performance is dependent on the width of the correlation rectangle. A small width decreases the chance for small, overlapping suspect regions appearing in the pair of images, while a large width increases that probability, yielding a higher number of false-positives. In this study, we used the smallest boundary width enclosing suspect regions to ensure that optimum performance may be obtained for pairs of projection images. However, this parameter can perhaps be more rigorously optimized in future implementations. Thirdly, it is possible that BCI performance might be somewhat dependent on the acquisition parameters. We have not explicitly studied such effects but expect them to be small, as the main limitation of nodule detection seems to be anatomical noise, a factor relatively invariable to acquisition parameters. Nonetheless,

**Fig. 9** BCI results reflective of the operational ranges of performance as a function of angular separation, for negative angular projections (a) and positive angular projections (b), averaged across all cases



such potential dependencies may need to be investigated. Finally, while the findings of this study suggest that CAD–BCI can be used as a possible effective method to reduce the number of false-positives for lung nodule detection in chest radiography, the focus of the study was primarily the establishment of the methodology and its feasibility based on phantom images and limited human subject cases. More cases will be needed to more rigorously evaluate the performance of CAD–BCI in clinical settings.

**Acknowledgments** This study is supported by grants from the NIH: R21CA91806, R01CA109074, and R01CA80490.

## References

- American Cancer Society: Cancer Facts and Figures. American Cancer Society, Atlanta, 2008
- Manning DJ, Ethell S, Donovan T: Detection or decision errors? Missed lung cancer from the posteroanterior chest radiograph. *Br J Radiology* 77:231–235, 2004
- White CS, Flukinger T, Jeudy J, Chen JJ: Use of a computer-aided detection system to detect missed lung cancer at chest radiography. *Radiology* 252:273–281, 2009
- Heelan RT, Flehinger BJ, Melamed MR, Zaman MB, Perchick WB: Non-small-cell lung cancer: Results of the New York screening program. *Radiology* 151:289–293, 1984
- Padilla J, Calvo V, Penalver JC, Sales G, Morcillo A: Surgical results and prognostic factors in early non-small cell lung cancer. *Ann. Thorac. Surg.* 63:324–326, 1997
- Revesz G, Kundel HL: Psychophysical studies of detection errors in chest radiology. *Radiology* 123:559–562, 1977
- Muhm JR, Miller WE, Fontana RS, Sanderson DR, Uhlenhopp MA: Lung cancer detected during a screening program using four-month chest radiographs. *Radiology* 148:561–565, 1983
- Gavelli G and Giampalma E: “Sensitivity and specificity of chest X-ray screening for lung cancer,” Proceedings of the International Conference on Prevention and Early Diagnosis of Lung Cancer. Varese, Italy, 1998, pp 103–108.
- Kundel HL, Nodine CF, Carmody D: Visual scanning, pattern recognition and decision-making in pulmonary nodule detection. *Investigative Radiology* 13:175–181, 1978
- Kundel HL, Nodine CF: Interpreting chest radiographs without visual search. *Radiology* 116:527–532, 1975
- Carmody DP, Nodine CF, Kundel HL: An analysis of perceptual and cognitive factors in radiographic interpretation. *Perception* 9:339–344, 1980
- Giger ML, Doi K, MacMahon H: Image feature analysis and computer-aided diagnosis in digital radiography, III: Automated detection of nodules in peripheral lung fields. *Med. Phys.* 15:158–166, 1988
- Doi K: Current status and future potential of computer-aided diagnosis in medical imaging. *Radiology* 78:S3–19, 2005
- Baydush AH, Floyd Jr, CE: Spatially varying Bayesian image estimation. *Acad Radiology* 3:129–136, 1996
- Lo SC, Freedman MT, Lin JS, Mun SK: Automatic lung nodule detection using profile matching and back-propagation neural network techniques. *J Digital Imaging* 6:48–54, 1993
- Burgess AE, Li X, Abbey CK: Nodule detection in two component noise: Toward patient structure. *SPIE Med. Imaging* 3036:2–13, 1997
- Samei E, Eyler WR, Baron LF: Effect of anatomical structure on signal detection. In: Beutel J, Van Metter R, Kundel H Eds. *Handbook of Medical Imaging*, vol. I Physics and Psychophysics. SPIE Press, Bellingham, 2000
- Revesz G, Kundel HL, Graber MA: The influence of structured noise on the detection of radiologic abnormalities. *Investigative Radiology* 9:479–486, 1974
- Neitzel U, Pralow T, Schaefer-Prokop C, Prokop M: Influence of scatter reduction on lesion signal-to-noise ratio and lesion detection in digital chest radiography. *Proceedings of SPIE Medical Imaging* 3336, 1998.
- Samei E, Catarious D, Baydush A, Floyd E, Vargas-Voracek R, “Bi-plane correlation imaging for improved detection of lung nodules,” *Proc SPIE Medical Imaging: Physics of Image Processing* 5030: 284–297 (2003).
- Samei E, Stebbins SA, Dobbins III, JT, Lo JY: Multiprojection correlation imaging for improved detection of pulmonary nodules. *AJR* 188:1239–1245, 2007
- Majdi Nasab N, Samei E, Dobbins JT: Biplane correlation imaging for lung nodule detection: Initial human subject results. *Proc. SPIE Medical Imaging* 6144:646–653, 2006
- Majdi Nasab N, Samei E: The impact of angular separation on the performance of biplane correlation imaging for lung nodule detection. *Proc. SPIE Medical Imaging* 6142:445–453, 2006
- Dobbins III, JT, Godfrey DJ: Digital X-ray tomosynthesis: Current state of the art and clinical potential. *Phys. Med. Biol.* 48:65–106, 2003
- Samei E, Flynn MJ, Eyler W: Simulation of subtle lung nodules in projection chest radiography. *Radiology* 202:117–124, 1997
- Jain AK: *Fundamentals of Digital Image Processing*. Prentice Hall, Englewood Cliffs, 1989
- Zheng B, Huang YH, Gur D: Computerized detection of masses in digitized mammograms using single-image segmentation and a multilayer topographic feature analysis. *Academic Radiology* 2:959–966, 1995
- Li SZ: Modeling image analysis problems using Markov random fields. In: Rao CR, Shanbhag DN Eds. *Stochastic Processes: Modeling and Simulation*. Elsevier Science Publishing Company, Amsterdam, 2000, pp 1–43
- Besag J: Spatial interaction and the statistical analysis of lattice systems. *J Royal Stat. Soc., Series B* 36:192–236, 1974
- Geman S, Geman D: Stochastic relaxation, Gibbs distributions and the Bayesian restoration of images. *IEEE Trans. on Pattern Analysis and Machine Intelligence* 6:721–741, 1984
- Majdi Nasab N, Analoui M, Delp EJ: Robust and efficient image segmentation approaches using Markov random field. *J Electron. Imaging* 12:50–58, 2003
- Majdi Nasab N and Analoui M: “Efficient multiresolution approach for image segmentation based on Markov random field,” *Proc. SPIE, Med. Imaging 2001: Image Processing* 4322: 1066–1074, 2001
- Lim JS: *Two-Dimensional Signal and Image Processing*. Prentice Hall, Englewood Cliffs, 1990, pp 536–540
- Chakraborty DP: Maximum likelihood analysis of free-response operating characteristic (FROC) data. *Med. Phys.* 16:561–568, 1989
- Stewart BK, Huang HK: Single-exposure dual-energy computed radiography. *Method Phys.* 17:866–875, 1990
- Kido S, Ikezoe J, Naito H, Arisawa J, Tamura S, Kozuka T, Ito W, Kato H: Clinical evaluation of pulmonary nodules with single-exposure dual-energy subtraction chest radiography with an iterative noise-reduction algorithm. *Radiology* 194:407–412, 1995
- Dobbins III, JT, McAdams HP, Song J-W, Li CM, Godfrey DJ, DeLong DM, Paik S-H, Martinez-Jimenez S: Digital tomosynthesis of the chest for lung nodule detection: Interim sensitivity results from an ongoing NIH-sponsored trial. *Med. Physics* 35:2554–2557, 2008

38. Dobbins III, JT, McAdams HP: Chest tomosynthesis: Technical principles and clinical update. *European J Radiology* 72:244–251, 2009
39. Henschke CI, McCauley DI, Yankelevitz DF, Naidich DP, McGuinness G: Early lung cancer action project: Overall design and findings from baseline screening. *Lancet* 354:99–105, 1999
40. Aoyama M, Li Q, Katsuragawa S, Li F, Sone S, Doi K: Computerized scheme for determination of the likelihood measure of malignancy for pulmonary nodules on low-dose CT images. *Med. Phys.* 30:387–94, 2003
41. Wisnivesky JP, Mushlin AI, Sicherman N, Henschke C: The cost-effectiveness of low-dose CT screening for lung cancer: Preliminary results of baseline screening. *Chest* 124:614–621, 2003
42. Gavrielides AM, Kinnard LM, Myers KJ, Petrick N: Noncalcified lung nodules. *Radiology* 251:26–371, 2009
43. El-Baz A, Gimel'farb GL, Falk R, El-Ghar MA: Automatic analysis of 3D low dose CT images for early diagnosis of lung cancer. *Pattern Recognition* 42:1041–1051, 2009
44. Reiser I, Sidky EY, Giger ML, Nishikawa RM, Rafferty EA, Kopans DB, Moore R, Wu T: A reconstruction-independent method for computerized lesion detection of mammographic masses in digital tomosynthesis images of the breast. *Proc. SPIE Med. Imaging* 5370:833–838, 2004
45. van Ginneken B, ter Haar Romeny BM, Viergever MA: Computer-aided diagnosis in chest radiography: A survey. *IEEE Trans. on Med. Imaging* 20:1228–1241, 2001
46. Doi K, MacMahon H, Giger ML, Hoffmann K: "Computed-Aided Diagnosis in Med. Imaging," (Ed) Elsevier, Amsterdam, The Netherlands, 1999, pp 11–20.
47. Giger M, MacMahon H: Image processing and computer-aided diagnosis. *Radiologic Clinics N. Amer.* 34:565–596, 1996
48. van Ginneken B, Katsuragawa S, ter Haar Romeny BM, Doi K, Viergever MA: Automatic detection of abnormalities in chest radiographs using local texture analysis. *IEEE Trans Med Imaging* 21:139–149, 2002
49. Giger ML, Doi K, MacMahon H, Metz CE, Yin F: Pulmonary nodules: Computer-aided detection in digital chest images. *RadioGraphic* 10:41–51, 1990
50. Penedo MG, Carreira MJ, Mosquera A, Cabello D: Computer-aided diagnosis: A neural-network-based approach to lung nodule detection. *IEEE Trans Med Imaging* 17:872–880, 1998
51. Kilday J, Palmieri F, Fox MD: "Classifying mammographic lesions using computerized image analysis," *IEEE Trans. on Med. Imaging* 664–669, 1993.
52. Haralick RM, Shanmugam K, Dinstein L: Textural features for image classification. *IEEE Trans Systems, Man, and Cybernetics* 3:610–621, 1973